

SCIENTIFIC REPORTS



OPEN

TiO₂ nanoparticles assembled on kaolinites with different morphologies for efficient photocatalytic performance

Xiaoyu Li¹ , Kang Peng² , Huaxin Chen¹ & Zhenjun Wang¹

Natural kaolinite clays with different dimensionalities (including kaolinite nanoflakes and nanorods) supported TiO₂ nanoparticles were successfully prepared via a facile sol-gel method. Moreover, comparisons between FK/TiO₂ and RK/TiO₂ nanocomposites are conducted in terms of matrix morphology, surface property, energy band structure and interfacial interaction. The effects of kaolinite microstructure, morphology and dimensionality on the interfacial characteristics and photocatalytic properties of the nanocomposites were investigated in detail. The results showed that TiO₂ nanoparticles are more easily attached on the kaolinite nanoflakes, and possess more uniform distribution and smaller particle size than that of kaolinite nanorods. In particular, the FK/TiO₂ nanocatalysts exhibit higher photocatalytic activity for the degradation of tetracycline hydrochloride than that of RK/TiO₂ and bare TiO₂, which is attributed to the stronger surface adsorptivity, higher loading efficiency and smaller grain size. Additionally, FK/TiO₂ composites show excellent stability, which is ascribed to the intimate interfacial contact between two-dimensional kaolinite nanoflakes and TiO₂ nanoparticles. Overall, the enhanced catalytic performance for FK/TiO₂ composites is the synergistic effect of two-dimensional morphology, better adsorption capability and more active photocatalysis TiO₂ species.

Heterogeneous nanocomposites has attracted increasing attention because of the synergetic properties and potential applications as green methods to solve the energy and environmental problems¹. In recent years, many technologies are proposed to tailor and promote the properties of nanocomposites, including element doping², surface loading³⁻⁶, morphology controlling⁷⁻¹¹, heterostructure constructing¹²⁻¹⁶, energy-band engineering¹⁷, and so on. Among them, loading functional nanoparticles on the surface of matrix materials is a promising alternative to control the nanoparticle size, and overcome inherent drawbacks of unsupported nanoparticles in terms of stability, agglomeration and reusability¹⁸.

As is well known, the performance of nanocomposites depends not only on the chemical composition, but also on microstructure, dimension, size and morphology and so on. At present, much interest has been focused on nanoparticles anchoring on a single support or the morphology-controlled synthesis of functional particles via different strategies, and further studied the comparative catalytic efficiency of the synthesized samples. Yang *et al.*¹⁹ synthesized a series of graphene-TiO₂ nanocomposites with different TiO₂ dimensionalities (including TiO₂ nanoparticles, nanotubes and nanosheets) via sol-gel method, alkaline hydrothermal process and one-step solvothermal method, respectively. Meshram *et al.*²⁰ reported synthesis of CuO nanostructures with different morphologies such as spherical, vesicular, nanosheet and platelet using chemical precipitation and hydrothermal methods. The photocatalytic activities of CuO nanostructures were evaluated by monitoring degradation of methylene blue, and the platelet-like CuO nanostructures were found to have the best catalytic activity. Thuy *et al.*²¹ prepared TiO₂ particles with different morphologies via hydrothermal process, and investigated the morphological effect of TiO₂ on photocatalytic degradation of organic dyes. However, none of these reports investigate any particular insights into the morphology of the support which has been reported to be as important as its internal structure. Like synthetic MCM-41, as common matrix materials²², have different morphologies, including mesoporous

¹School of Materials Science and Engineering, Chang'an University, Xi'an, 710064, China. ²State Key Laboratory for Mechanical Behavior of Materials, Xi'an Jiaotong University, Xi'an, 710049, China. Correspondence and requests for materials should be addressed to X.L. (email: leexy@chd.edu.cn) or K.P. (email: pengkangtm@xjtu.edu.cn)

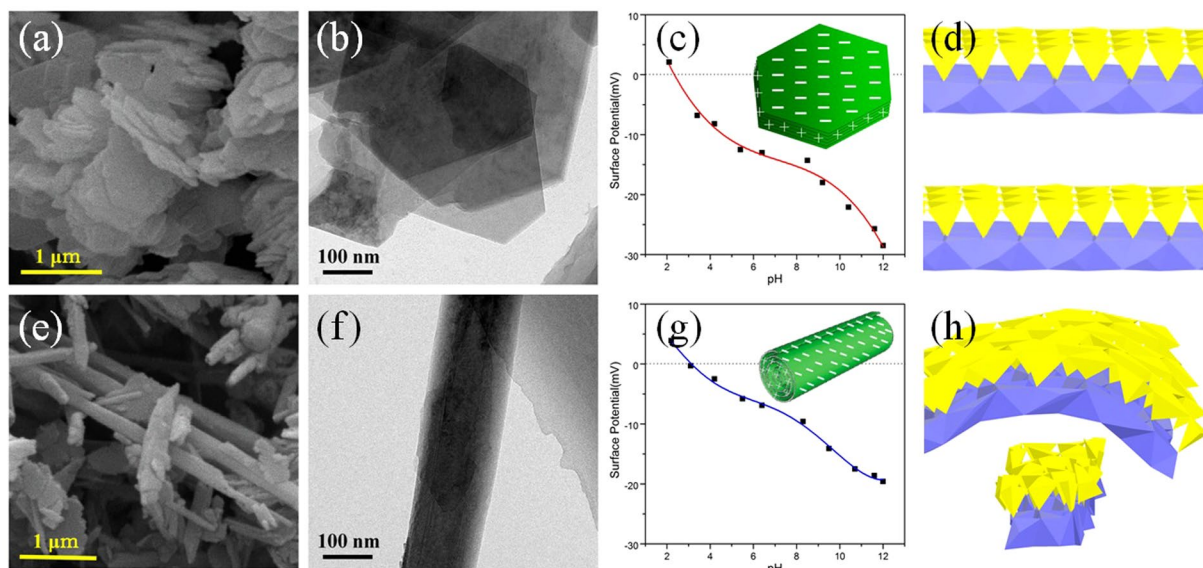


Figure 1. Morphology and schematic drawing of the samples. SEM, TEM images and Zeta potential (the insets are the schematic view of surface charge distributions) of (a–c) FK, (e–g) RK. Schematic drawing of the crystal structures of (d) FK and (h) RK as a combination of AlO_6 octahedra with SiO_4 tetrahedra.

silica nanoparticles²³, nanofibers²⁴, nanotubes²⁵, ordered hollow spheres²⁶ or core-shell structured spheres²⁷. It is significant to select an optimum morphology for a support to prepare a more efficient and reusable catalyst in a green process.

Kaolinite [$\text{Al}_2\text{Si}_2\text{O}_5(\text{OH})_4$] is a 1:1-type clay mineral composed of stacked layers of SiO_4 tetrahedral sheets and $\text{AlO}_2(\text{OH})_4$ octahedral sheets²⁸ and naturally possesses diverse morphologies, including one-dimensional (nanotubes and nanorods) and two-dimensional morphology (nanoflakes)²⁹. The schematic drawing of the crystal structures of kaolinite nanoflakes and kaolinite nanorods as a combination of AlO_6 octahedra with SiO_4 tetrahedra is shown in Fig. 1d,h. Meanwhile, kaolinite clays possess plentiful hydroxyl groups on the surface, which is beneficial to surface modification and make kaolinite become a suitable matrix for anchoring of TiO_2 nanoparticles to enhance the photocatalytic activity. Zhang *et al.*³⁰ successfully synthesized TiO_2 /kaolinite composites with mixed phase TiO_2 (anatase and brookite) at low temperature. The crystal type of TiO_2 nanoparticles could be controlled by the kaolinite matrix, and finally improve the catalytic performances. Hai *et al.*³¹ prepared acid-activated kaolinite via calcination and acid activation of coal-bearing kaolinite and then modified with TiO_2 nanoparticles to improve its ability to adsorb and hence remove azo dyes. Kutlakova *et al.*³² prepared nanocomposite kaolinite/ TiO_2 using thermal hydrolysis of titanyl sulfate (TiOSO_4) in the presence of kaolin, and calcined kaolinite/ TiO_2 at 600 °C. Thermal treatment was beneficial to the improvement of the photocatalytic activity of kaolinite/ TiO_2 composites. These studies are inclined to focus on the crystal structure changes of TiO_2 on a substrate, but ignore the effect of matrix morphology on properties of TiO_2 . Therefore, preparing catalysts with kaolinites possessing the natural different morphologies is a very meaningful study to clarify the effect of clays dimensionality on the photocatalytic behavior and interfacial characteristics of kaolinite/ TiO_2 nanostructures.

In this work, based on the features of kaolin clays, unique layered structure, with similar chemical composition, but natural different morphologies (one-dimensional nanorods and two-dimensional nanoflakes), we have successfully assembled uniform TiO_2 nanoparticles on the surface of kaolinite clays by a facile sol-gel method. The effects of kaolinite clays microstructure and dimensionality on the interfacial characteristics and catalytic properties of the composites were investigated in detail. TiO_2 nanoparticles were efficiently deposited on the surface of kaolinites. The photocatalytic activity of this porous material was evaluated by tetracycline hydrochloride degradation. The clays/ TiO_2 simultaneously covered their excellent properties of TiO_2 and kaolinites, exhibited high photocatalytic activity and adsorption property, and endowed this material with a bright perspective in degradation of antibiotics.

Results

Morphological and structural characteristics. The general morphologies of different samples were observed by electron microscope. Typical SEM and TEM analysis indicates that kaolinite clays used in the experiments naturally possess different morphologies, and the kaolinite particles all possess smooth surface without contamination (Fig. 1a,b,e,f). Kaolinite nanoflakes exhibit an irregular angular shape and the length of particles are in the range of microns (Fig. 1a,b). Nanorod-like kaolinites with smooth surface (Fig. 1e,f) are mostly 2–5 μm in length and 0.1–0.3 μm in diameter with a length to width ratio of about 20:1. It can be seen from Fig. 2d, bare TiO_2 nanoparticles are obtained via the sol-gel method combined heat treatment. However, the dispersion of bare TiO_2 nanoparticles is poor and exists obvious aggregation. In the presence of clays, the aggregation of TiO_2 nanoparticles is markedly inhibited (Fig. 2a,e) and TiO_2 nanoparticles are uniformly deposited on the surface

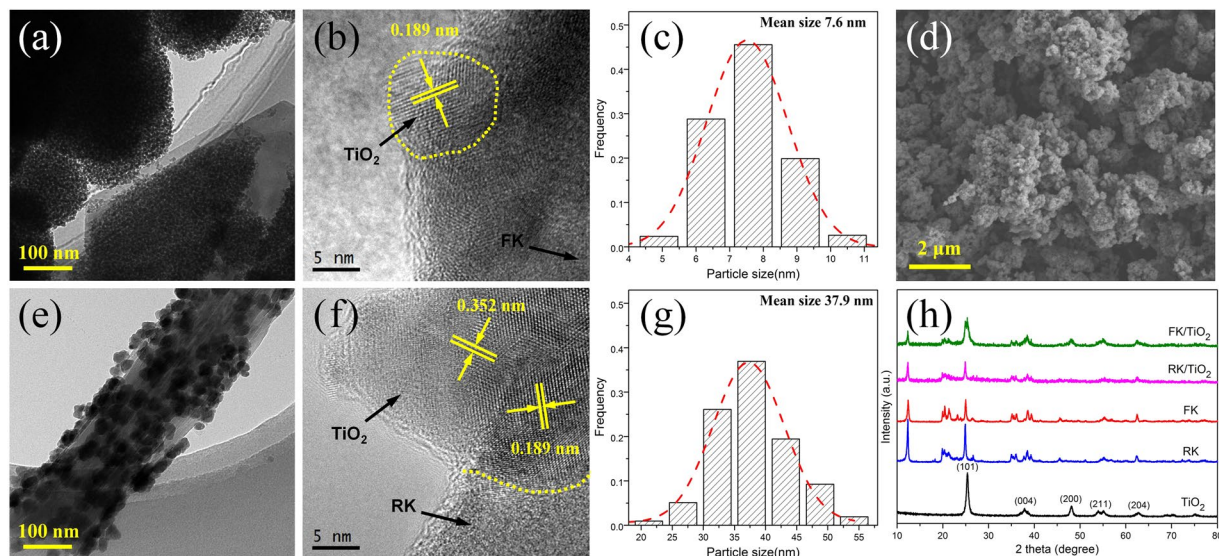


Figure 2. Morphology and crystallization of the samples. TEM, HRTEM images and the corresponding histograms of TiO_2 clusters diameters of (a–c) FK/ TiO_2 , (e–g) RK/ TiO_2 . (d) SEM image of bare TiO_2 aggregates, (h) XRD patterns of different samples.

of clays. After loading TiO_2 nanoparticles, the clay supports show different loading results at the same experiment conditions. The TiO_2 nanoparticles exhibit much more uniform and smaller for FK/ TiO_2 (Fig. 2a) and aggregation seriously for RK/ TiO_2 (Fig. 2e), which indicates that the morphology of supports have a seriously effect on the particles size. The HRTEM (Fig. 2b,f) results indicate that TiO_2 nanoparticles have high crystallinity with well-defined lattice fringes of 0.189 nm corresponding to (200) plane, and 0.352 nm corresponding to (101) plane, in accordance with XRD results (Fig. 2h). Moreover, obvious interfaces are observed between the TiO_2 and clays. The intimate interaction enables the electron to more easily transfer from TiO_2 nanoparticles to kaolinite nanoflakes during the photoexcitation process. Meanwhile, the mean size of TiO_2 nanoparticles for FK/ TiO_2 and RK/ TiO_2 measured on TEM images (Fig. 2a,e) are 7.6 and 37.9 nm, respectively, as shown in Fig. 2c,g. It is clear that the grain size of TiO_2 nanoparticles is strongly depended on the morphology of the supports. Meanwhile, the TiO_2 nanoparticles on kaolinite clays are much smaller than that of bare TiO_2 (Fig. 2d), indicating the dispersion effect on TiO_2 clusters on the surface of kaolinite clays. The measured surface zeta potential curves and the surface charge distributions sketches of pristine kaolinites with different morphologies are showed in Fig. 1c.g. It is clear that kaolinites with different morphologies carry a net negative charge, which allows for its good dispersibility in water and provided a strong electrostatic adsorption force to the positively charged molecules on the surfaces. But they possess the different surface charge distributions, thus leading to the different surface natures, which allows the adjustable grain size of TiO_2 nanoparticles and further affects the photocatalytic performances.

As a result, the kaolinite clays with different morphologies can serve as supporting materials for *in situ* growth of TiO_2 nanoparticles. The TiO_2 nanocrystals attached on kaolinite nanoflakes have better dispersion and much smaller grain size than that of RK/ TiO_2 and bare TiO_2 samples, resulting from the intimate interaction and good interfacial contact. Therefore, the TiO_2 particles size can be controlled by clays and form interaction with clays surface, which would lead to exposing more catalytic reaction sites, improving photoelectrons transiting and enhancing the photocatalytic activity.

Figure 2h shows the XRD patterns of as-synthesized samples to study the crystal structure and crystalline phase of TiO_2 in the nanocomposites. It can be clearly seen that kaolinite clays possessed the natural different morphologies have the similar crystal structure and their XRD patterns are in good agreement with the standard PDF card of JCPDS 14-0164 for kaolinite-1A³³. The XRD pattern of bare TiO_2 shows the highly crystalline anatase phase TiO_2 (JCPDS No. 21-1272)³⁴. The diffraction peaks of FK/ TiO_2 and RK/ TiO_2 composites are in good agreement with the anatase phase TiO_2 and kaolinite, showing that the structure of kaolinite is maintained during the introduction of TiO_2 nanoparticles. Meanwhile, the diffraction intensities of kaolinites in FK/ TiO_2 and RK/ TiO_2 composites are decreased, indicating the successful loading of TiO_2 on the surface of kaolinites. The average grain size of TiO_2 nanoparticles for FK/ TiO_2 and RK/ TiO_2 estimated by the Scherrer's formula are 9.1 and 32.4 nm, respectively, which is consistent with the results based on TEM images. Moreover, the grain size of bare TiO_2 is 16.8 nm. By comparison to the standard JCPDS diffraction patterns of anatase phase TiO_2 , it can be seen that the diffraction peaks of TiO_2 on FK/ TiO_2 are much more obvious than that of RK/ TiO_2 , which indicates that FK has relatively higher loading efficiency for TiO_2 nanoparticles at the same experiment conditions. In order to further confirm the results, elemental analysis (Table 1) was employed in the experiment. It is shown that the relative content of titanium in FK/ TiO_2 is higher than that of RK/ TiO_2 , which is consistent with the XRD results.

The nitrogen adsorption-desorption isotherms of different samples and BJH pore size distribution are shown in Fig. 3, and the textural parameters calculated from the corresponding isotherms are summarized in Table 2. As shown in Fig. 3a, the adsorption-desorption isotherms of bare TiO_2 almost have no hysteresis loop, and the

Samples	SiO ₂	Al ₂ O ₃	Fe ₂ O ₃	CaO	MgO	TiO ₂	K ₂ O	Na ₂ O	Ig.loss
FK	46.90	38.14	0.15	0.01	0.11	0.14	0.30	0.19	13.98
RK	46.78	38.51	0.96	0.04	0.03	0.05	0.19	0.02	13.82
FK/TiO ₂	23.75	19.14	48.21	0.11	0.01	0.06	0.21	0.12	8.39
RK/TiO ₂	29.51	20.32	42.16	0.53	0.02	0.01	0.11	0.01	7.33

Table 1. The chemical composition of different samples (mass %).

Material	S_{BET} (m ² /g)	V_{pores} (cm ³ /g)	d_{pores} (nm)	Band gap energy (eV)
FK	27	0.09	11.8	—
RK	26	0.06	9.2	—
FK/TiO ₂	114	0.25	8.7	3.21
RK/TiO ₂	109	0.35	12.5	3.19
TiO ₂	13	0.04	11.4	3.20

Table 2. The textural characteristics of all samples. Notes: S_{BET} = BET specific surface area, V_{pores} = total pore volume, d_{pores} = average pore diameter.

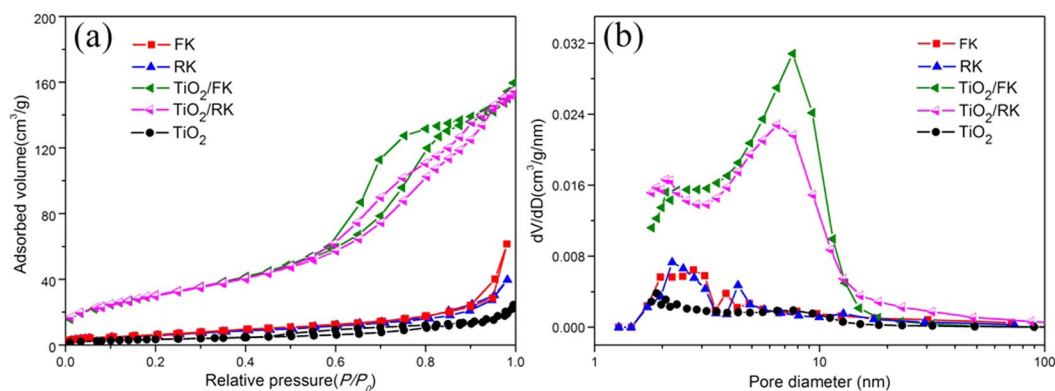


Figure 3. Textural characteristics of the samples. (a) Nitrogen adsorption-desorption isotherms, (b) corresponding BJH pore size distribution of different samples.

BET specific surface area is only 13 m²/g due to the seriously aggregation, while the adsorption-desorption isotherms of clays/TiO₂ exhibit typical characteristic of type-IV with distinct type H3 hysteresis loop, indicating the formation of mesoporous structures³⁵. However, the adsorption-desorption isotherms of clays almost have no hysteresis loop, and the specific surface area are only about 27 m²/g, indicating clays nanoparticles can easily aggregate and result in the performance decline. After supporting TiO₂ nanoparticles on the surface of clays, the BET specific surface area (S_{BET}) and pore volume (V_{pores}) of composites are increased, as summarized in Table 2. It shows that the mesopore structure can be formed after loading TiO₂ nanoparticles by revealing increased surface area from 27 to 114 m²/g for FK/TiO₂, and from 26 to 109 m²/g for RK/TiO₂. The pore volume of FK/TiO₂ and RK/TiO₂ are 0.25 and 0.35 cm³/g, respectively. Obviously, FK/TiO₂ has relatively higher specific surface area and lower pore volume, compared with RK/TiO₂, which might be because the smaller size and uniform distribution of TiO₂ nanoparticles attached on kaolinite nanoflakes. These results are further confirmed by the observation from their pore size distribution calculated by BJH method (Fig. 3b). These characteristics seem to be responsible for enhanced catalytic activity and stability on the clays/TiO₂ in comparison with bare TiO₂. These properties are also attributed to the formation of small particles through oxide-support interaction to provide more active sites for photocatalysts.

Interfacial characteristics. The surface properties of TiO₂ species play an important role in aqueous phase photocatalytic reaction, and a large surface area of FK/TiO₂ is responsible for the efficient catalytic activity. In addition, the interactions between TiO₂ and clays are also important to suppress the aggregation of TiO₂ nanoparticles during the reaction, and the oxide-support interactions are measured by FTIR and XPS, which can provide additional information on the structure of clays/TiO₂ nanocomposites.

The FTIR spectra of the samples are shown in Fig. 4a to analyze the vibrational bands and the interface interaction. For FK and RK, the peak at 1033 cm⁻¹ corresponds to the stretching vibration of the skeleton Si-O network (Si-O-Si and O-Si-O)³⁶. The broad band between 1631 cm⁻¹ is assigned to adsorbed water. The other bands at 3658 and 1116 cm⁻¹ are assigned to inner surface hydroxyl out-of-phase stretching vibration and apical

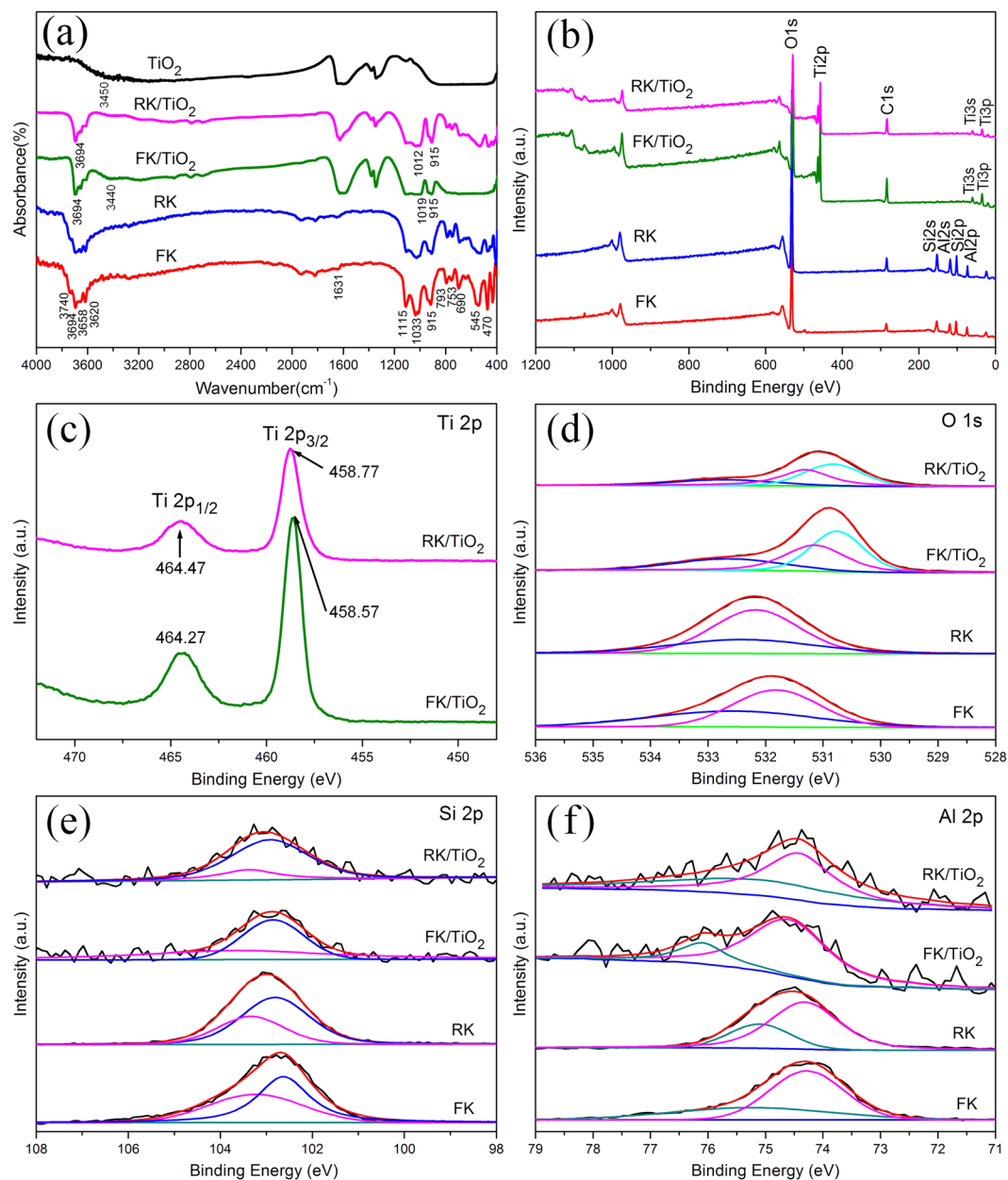


Figure 4. Interfacial characteristics of the samples. (a) FTIR spectra and (b) XPS survey spectra of different samples. (c) Ti 1 s, (d) O 1 s, (e) Si 2p and (f) Al 2p fitted XPS spectra of different samples.

Si-O stretching vibration, respectively. The absorption bands at 3694, 3620, and 915 cm^{-1} are ascribed to an inner-surface hydroxyl (Al-OH) stretching vibration, which are rarely influenced by intercalation²⁹. The peak at 3740 cm^{-1} is assigned to the outer-surface hydroxyl (Si-OH) stretching vibrations. The bands at 793, 753 and 690 cm^{-1} are due to the translational vibration of O-Al-OH. Meanwhile, the bands at 545 and 470 cm^{-1} are attributed to the vibration of Si-O-Al. There is little change in the band positions of RK compared with FK, only the overall intensity are slightly reduced. FK/TiO₂ and RK/TiO₂ show the characteristic bands of kaolinite at 3694, 1116 and 915 cm^{-1} and TiO₂ at between 1600 and 1200 cm^{-1} . The absorption band at 3740, 3658 and 3620 cm^{-1} ascribed to surface hydroxyl groups vibration are disappeared, indicating the structural dehydroxylation of the kaolinite, which might be caused by immobilization of TiO₂ nanoparticles on the surface of kaolinite or the bonding on Ti atoms on these sites, leading to a reduction of hydroxyl groups. The Si-O stretching band at about 1033 cm^{-1} , which shifts to 1019 and 1012 cm^{-1} for FK/TiO₂ and RK/TiO₂, respectively. The shifting of the skeleton Si-O network stretching band indicates the formation of hydrogen bonding between the outer surface of the kaolinites (tetrahedral sheet) and TiO₂. Moreover, the new broad band around 3440 cm^{-1} is assigned to Ti-O and its intensity for FK/TiO₂ is higher than that of RK/TiO₂. Furthermore, the bands at 793, 753, 690, 545 and 470 cm^{-1} are disappeared for FK/TiO₂, while still remained for RK/TiO₂. These results provide evidences for the existence of interaction between kaolinite and TiO₂ and confirm that the FK can be coated by TiO₂ nanoparticles

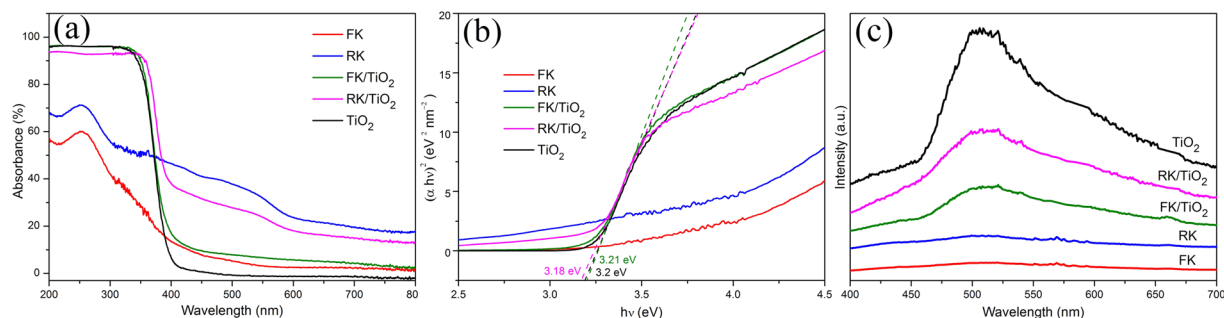


Figure 5. Optical spectroscopic study of the samples. **(a)** UV-vis diffuse reflectance spectra of different samples, **(b)** the corresponding plots of $(\alpha hv)^2$ vs. photon energy ($h\nu$). **(c)** The photoluminescence spectra of different samples.

much more effectively and the binding force is much stronger than that of RK, which is consistent with the TEM (Fig. 2) and XRF results (Table 1).

The interactions between TiO_2 and kaolinite clays in the composites are further investigated by using XPS spectra. Figure 4b shows the XPS survey spectra of FK, RK, FK/ TiO_2 and RK/ TiO_2 in the range 0–1200 eV. The XPS survey spectra of FK/ TiO_2 and RK/ TiO_2 clearly identify the signals of the Al, Si, Ti and O elements. The weak signals of Si and Al elements for clays/ TiO_2 indicate that the kaolinites surface are coated with a layer of dense nano-sized TiO_2 particles.

The high-resolution XPS spectra of Ti 2p, O 1s, Si 2p and Al 2p for samples are exhibited as Fig. 4c–f, respectively. As shown in the high-resolution spectra of Ti 2p electrons (Fig. 4c), two bands located at 458.77 and 464.47 eV for RK/ TiO_2 , and 458.57 and 464.27 eV for FK/ TiO_2 can be assigned to $\text{Ti } 2p_{3/2}$ and $\text{Ti } 2p_{1/2}$ spinorbital splitting photoelectrons in the Ti^{4+} chemical state, respectively³⁷. Meanwhile, Ti^{4+} combines with kaolinites and forms Si–O–Ti bond³⁷. This interaction of chemical bond can immobilize TiO_2 to prevent it from movement and agglomeration. The slight shifts for FK/ TiO_2 and RK/ TiO_2 can be due to a change in the chemical state or coordination environment of Ti 2p, that is, the interaction between kaolinites with different morphologies and TiO_2 nanoparticles. Moreover, the larger peak area of Ti 2p for FK/ TiO_2 indicates that TiO_2 nanoparticles are more easily loaded onto the surface of the flake-like support under the same condition.

The high resolution O 1s spectra of kaolinites can be deconvoluted into two fitted peaks (Fig. 4d). The peak at around 532.6 eV can be assigned to lattice oxygen in the kaolinites, and the other peak at about 531.7 eV is derived from the hydroxyl group³⁸. For clays/ TiO_2 , the peaks at 532.6 eV and 530.6 eV are assigned to oxygen from Si–O–Si and Ti–O–Si, and the peak at 531.2 eV is assigned to oxygen from hydroxyl group. The result is in good consistent with that of Ti 2p (Fig. 4c) and confirms the existence of Ti–O–Si and surface hydroxyl. Moreover, the shifts of surface hydroxyl groups and the new formed Ti–O–Si demonstrate the integration between TiO_2 and kaolinites and intense interaction between the two components. Moreover, the larger peak area of Ti–O–Si for FK/ TiO_2 further indicates FK/ TiO_2 has relatively higher loading efficiency of TiO_2 nanoparticles than that of RK/ TiO_2 .

Figure 4e,f shows the Si 2p and Al 2p spectra of different samples, and the peak positions for kaolinites are observed at 103.3 eV (Si–OH), 102.7 eV (Si–O), 75.1 eV (Al–OH) and 74.3 eV (Al–O), respectively³⁹. After supporting TiO_2 nanoparticles on the surface of clays, the reduction of hydroxyl groups and slightly shifts for clays/ TiO_2 nanocomposites indicate the interaction between the two components.

Optical spectroscopic study. The UV-vis diffuse reflectance spectra are used to determine the optical properties of the synthesized samples. As shown in Fig. 5a, the FK and RK show clear absorption in the UV region, and a visible light absorption around 500 nm for RK can be observed. It is obvious that bare TiO_2 nanoparticles have no or relatively weak visible light absorption, while clays/ TiO_2 nanocomposites exhibit enhanced light absorption capacity in the UV-vis region, indicating that the weak absorption in the visible light region can be attributed to the kaolinites. In comparison to kaolinites, the absorptions attributed to crystalline TiO_2 around 400 nm are present, which further confirms that the crystalline TiO_2 nanoparticles are successfully attached on the surface of kaolinites in clays/ TiO_2 nanocomposites. Meanwhile, the positions of adsorption onsets of clays/ TiO_2 nanocomposites exhibit a significant shift compared to bare TiO_2 nanoparticles, which is due to the quantum size effect and dispersion effect of kaolinites. The shift of adsorption edge for FK/ TiO_2 is stronger than RK/ TiO_2 . It might be due to the smaller size of TiO_2 in FK/ TiO_2 , which is well consistent with the TEM results (Fig. 2).

The bandgap energy of clays/ TiO_2 samples can be confirmed roughly according to the plot of $(\alpha hv)^2$ versus energy ($h\nu$) of absorbed light (Fig. 5b), which is obtained on the basis of the Kubelka–Munk function ($F(R_\infty) = (1 - R)^2 / (2R)$), where α , h , ν and R are absorption coefficient, Planck constant, light frequency and reflectance with the reflectance at 1000 nm set at 100%, respectively. As shown in Fig. 5b, the band gap energies of the TiO_2 species in FK/ TiO_2 and RK/ TiO_2 are 3.21 and 3.18 eV, respectively. For comparison, the bandgap energy of bare TiO_2 nanoparticles, calculated from the corresponding plot of $(\alpha hv)^2$ vs. photon energy ($h\nu$), is 3.2 eV. The results indicate that FK/ TiO_2 possesses larger band gap energy, which can be attributed to the smaller grain size and the more intense interaction between TiO_2 and FK. It is conducive to the enhancement of photocatalytic performances.

The photoluminescence (PL) spectra of the samples at the excitation wavelength of 254 nm are shown in Fig. 5c. The PL peaks of clays/ TiO_2 are much lower than that of bare TiO_2 , thus suggesting the less recombination of photogenerated electrons and holes, which would lead to improved photocatalytic activity. FK/ TiO_2 nanocomposites have the intimate and uniform interfacial contact, in which photogenerated electrons from TiO_2

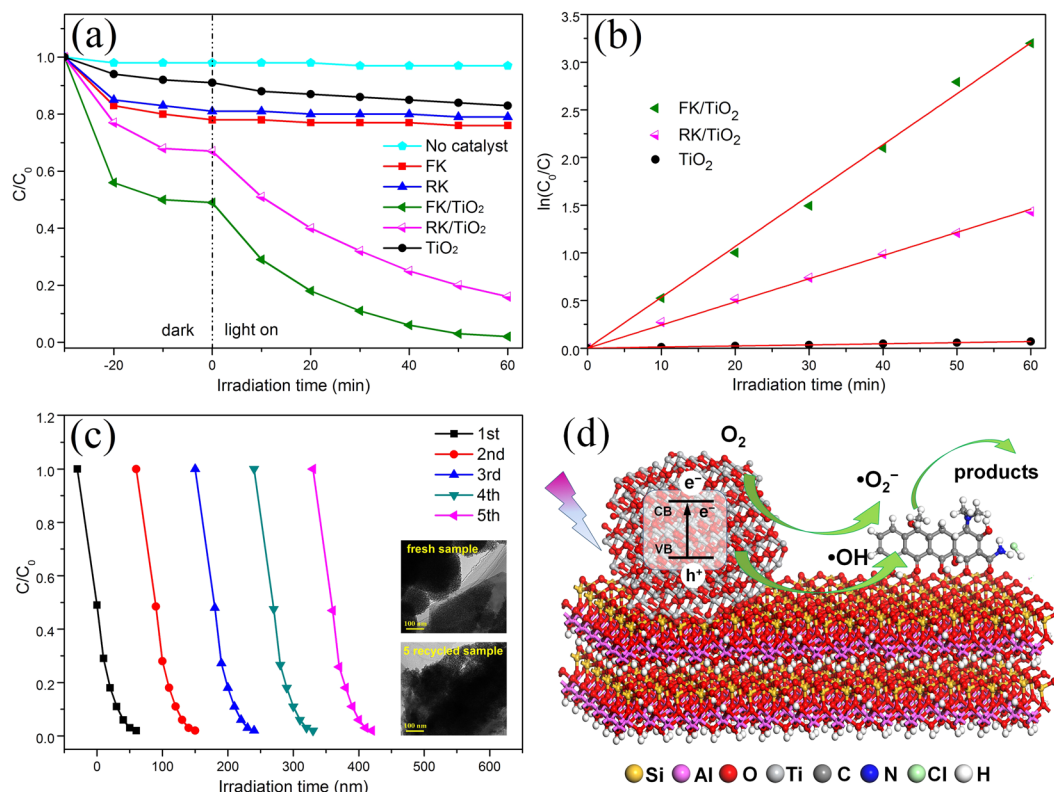


Figure 6. Photocatalytic properties and reaction mechanism of the samples. (a) Photocatalytic degradation curves of different samples, (b) pseudo-first-order plot with FK/TiO₂, FK/TiO₂ and bare TiO₂ nanoparticles. (c) Reusability of FK/TiO₂ nanocomposite for photocatalytic decomposition of tetracycline hydrochloride (the insets are the TEM images of fresh and recycled samples). (d) Schematic illustration of photocatalytic reaction mechanism of clays/TiO₂ nanocomposites.

conduction-band are injected rapidly into FK across the particles-nanosheets heterostructure interface. The smaller particles size and more efficient charge separation is achieved and consequently leads to higher photocatalytic activity, compared with RK/TiO₂ and bare TiO₂ nanoparticles.

Photocatalytic properties. The photocatalytic performances of as-prepared photocatalysts were measured to degrade antibiotics under UV light irradiation (Fig. 6). Figure 6a shows the degradation curves of tetracycline hydrochloride using FK, RK, FK/TiO₂, RK/TiO₂ and bare TiO₂ photocatalysts. For the blank experiment analysis, the result shows that tetracycline hydrochloride can be hardly degraded after 60 min under UV light irradiation without catalysts, excluding the possibility of self-photolysis in this system. The bare TiO₂, FK and RK exhibit 9, 22 and 19% of tetracycline hydrochloride adsorption after 30 min dark adsorption equilibrium, respectively. Upon UV light irradiation, the tetracycline hydrochloride can be slightly degraded with bare TiO₂, while there is no degradation by FK and RK. The photodegradation activity is enhanced by supporting TiO₂ nanoparticles on the kaolinites, and FK/TiO₂ composites show the highest photodegradation activity. After irradiation for 60 min, the photodegradation rate of FK/TiO₂ composite is 98%, but only 84% for the RK/TiO₂. It is reported that photocatalytic decomposition of tetracycline hydrochloride follows the pseudo-first-order reaction kinetics⁴⁰. As shown in Fig. 6b, the rate constant for bare TiO₂ is very small compared to that for clays/TiO₂ composites, and the rate constant of FK/TiO₂ is higher than that of RK/TiO₂. The enhanced photocatalytic activity for FK/TiO₂ composite can be attributed to the large surface area, decreased particle size and increasing density of active sites.

The stability and recyclability of FK/TiO₂ nanocomposite were evaluated by monitoring the reactivity of FK/TiO₂ during five reaction cycles. As shown in Fig. 6c, the photocatalytic activity of FK/TiO₂ can be easily recovered, and the photodegradation activity has no obvious decrease after five successive cycles. Moreover, the postmortem study shows that there is no significant changes for the supported structure of FK/TiO₂ after five reaction cycles, which indicates FK/TiO₂ has good stability. The good stability of FK/TiO₂ catalyst could be ascribed to the intense interaction between TiO₂ and FK, which can immobilize the active sites in photocatalysis. The well stability would greatly promote their practical application to eliminate the antibiotics.

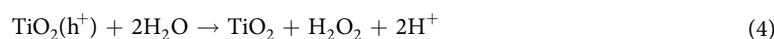
Discussions

Based on the above results, a possible mechanism to explain the enhancement of the photocatalytic properties of the clays/TiO₂ nanocomposites is depicted in Fig. 6d. The proposed mechanism is the synergetic effects between the kaolinite clays and supported TiO₂ nanoparticles. The TiO₂ clusters act as a light absorber, while the kaolinite clays with different morphology are the physical adsorbents of tetracycline hydrochloride molecules. In the dark,

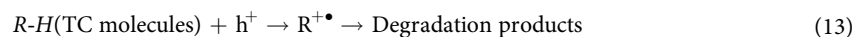
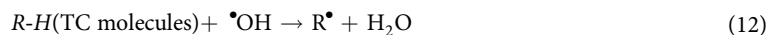
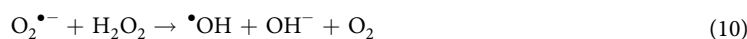
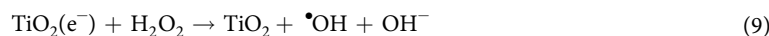
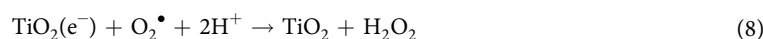
tetracycline hydrochloride molecules could be effectively adsorbed around the clays/TiO₂ nanocomposites and reach adsorption-desorption equilibrium on their surface, which could facilitate the photocatalytic reactions. TiO₂ nanoparticles supported on the clays could be excited to yield electrons (e⁻) and holes (h⁺) (Eq. (1)). These photo-induced electrons-holes reacted with oxygen molecules (O₂), H₂O or hydroxyl groups on the surface of kaolinites to yield hydroxyl radicals (•OH) and superoxide radical anions (O₂^{•-}) (Eq. (2–11))⁴¹. These active species with strong oxidizability directly or indirectly interacted with tetracycline hydrochloride molecules already adsorbed on FK/TiO₂ and RK/TiO₂ in aqueous solutions (Eq. (12–13))³⁷. The complete equations of mechanism reactions are as follows:



Reaction involving valence band h⁺



Reaction involving conduction band e⁻



Above-mentioned photocatalytic mechanism for tetracycline hydrochloride photodegradation, the surface adsorption and light-induced charge transfer are two primary factors affecting the photocatalytic activity. Strong adsorptivity contributes to the concentration of antibiotics from the solvent and consequently improves the photocatalytic activity. By comparison with FK/TiO₂ and RK/TiO₂ nanocomposites, FK/TiO₂ exhibits much stronger surface adsorption, compared to that of RK/TiO₂, which can originate from the large specific surface area. Moreover, the TiO₂ nanoparticles exhibit much more uniform and smaller for FK/TiO₂, while aggregation seriously for RK/TiO₂, and FK/TiO₂ has relatively higher loading efficiency of TiO₂ nanoparticles than that of RK/TiO₂, which can result in higher light-induced charge transfer, and finally enhance the photocatalytic activity. It is clear that the efficient photodegradation performance of FK/TiO₂ can be attributed to the synergistic effect of better adsorption capability and more active photocatalysis TiO₂ species. The specific surface area and the grain size of TiO₂ nanoparticles are strongly depended on the morphology of the kaolinite supports. Therefore, it is important to develop advanced technologies to control the particles morphology so that to enhance the catalytic performances.

In summary, this paper proposed a facile sol-gel method to synthesize clays/TiO₂ nanocomposites with high catalytic activity and stability. Based on the natural different morphologies and unique layered structure, the efficient assembly and high-density dispersion of uniform TiO₂ nanoparticles were successfully achieved on the surface of kaolinite clays. Degradation of antibiotics using clays/TiO₂ catalysts was investigated to elucidate the effects of kaolinite microstructure, morphology and dimensionality for a significant suppression of the TiO₂ nanoparticle aggregation during the reaction. FK/TiO₂ exhibited remarkably enhanced photoactivities toward degradation of tetracycline hydrochloride, and the overall degradation rate was up to 98% after light irradiation for 60 min. It could be attributed to the two-dimensional morphology, stronger surface adsorptivity, higher loading efficiency, smaller grain size and intimate interfacial contact. Therefore, our insight into the comparison of different dimensionality of kaolinite clays to photocatalytic performance could be a reference function to the similar investigation, and clays/TiO₂ composites have great potential applications to eliminate effectively antibiotics.

Methods

Materials. The kaolinite used was raw kaolin obtained from Fujian and Guangdong, China. The chemical compositions of flake-like kaolinite (FK) and rod-like kaolinite (RK) were listed in Table 1 and showed that kaolinites with different morphologies possessed the similar chemical composition. Other reagents were purchased from Sinopharm Chemical Reagent Co. Ltd. All reagents were analytical grade and used without further purification.

Preparation. TiO₂/kaolinite nanocomposite materials were prepared through a facile precipitation method. In a typical synthesis, 0.2 g kaolinite was added to a mixture constituted by 30.0 mL of ethanol and 0.6 mL of deionized water under dispersing in the ultrasonic bath for 30 min. Subsequently, 3 mL of tetrabutyl titanate (TBOT) dissolved in 5 mL of ethanol were put drop-wise into the kaolinite suspensions. After continuous stirring for 2 h at 80 °C, the precipitates were collected by centrifugation and subsequently washed with deionized water repeatedly. The resultant products were dried overnight at 80 °C. Finally, the samples were calcined under 450 °C for 3 h in air with a heating rate of 5 °C/min. For comparison, the bare TiO₂ nanoparticles were also obtained via a similar process as TiO₂/kaolinite composite without adding kaolinite.

Photocatalytic degradation experiments. The photocatalytic activity of the catalysts for tetracycline hydrochloride was investigated at ambient temperature. In a typical process, 50 mg of catalyst was dispersed in 50 mL of 30 mg/L tetracycline hydrochloride solution. The suspension was vigorously stirred in the dark for 30 min to reach the adsorption-desorption equilibrium, and then irradiated with ultraviolet light. Afterwards, 2.5 mL aliquots of the reaction mixtures were collected and the catalyst was removed from the solution using a 0.45 μm cellulose acetate membrane filter. The tetracycline hydrochloride concentrations in the filtrates were measured at 380 nm using the UV-vis spectrophotometer. The stability of catalyst was evaluated by the catalytic cycle test. At the end of each cycle, the suspension was filtered and the catalyst was tested in the next cycle.

Characterization. The chemical composition of kaolinite minerals and nanocomposites were determined using X-ray fluorescence (XRF) spectrometer. The structural characteristics of the samples were examined by X-ray diffraction (XRD, Rigaku D/MAX2550VB+) using Cu K α radiation ($\lambda = 0.15406$ nm) at a scanning rate of 0.02 °/s with a voltage of 40 kV and 40 mA. The microstructures of the samples were observed using a scanning electron microscopy (SEM, FEI Quanta-200) with an accelerating voltage of 5 kV, a transmission electron microscopy (TEM, JEOL JEM-2100F) and high-resolution transmission electron microscopy (HRTEM, JEOL JEM-3010) operating at 200 kV. The TiO₂ clusters were identified by X-ray photoelectron spectroscopy and their size distributions were determined by counting the sizes of TiO₂ clusters on TEM images taken from different places. The textural properties of the samples were determined by N₂ porosimetry. The N₂ adsorption-desorption isotherms were recorded at 77 K and analyzed using an ASAP 2020 Surface Area analyzer (Micromeritics Co. Ltd.). The specific surface areas were calculated using the Brunauer-Emmett-Teller (BET) equation, and estimates of the pore size distributions were deduced by means of Barrett-Joyner-Halenda (BJH) methods. The zeta potential of the samples at different pH levels was measured on a zeta potential analyzer (Zetasizer Nano ZS90, Malvern) at solids content of about 0.1% in distilled water. The interface characteristics and their chemical nature were studied by Fourier transform infrared (FTIR, Nicolet Nexus 670) and X-ray photoelectron spectroscopy (XPS, ESCALAB 250). Diffuse reflectance ultraviolet-visible (UV-vis) spectra were obtained on a Hitachi (Shimadzu) Model UV-2450 spectrophotometer. The Photoluminescence (PL) spectra were measured on a Hitachi F-4500 fluorescence spectrometer at room temperature using a Xe lamp with a wavelength of 254 nm as the excitation source. For the photocatalytic activity evaluation, a 150 W Xe lamp equipped with an optical cutoff filter ($\lambda < 400$ nm) was used as the light source, and the concentration of photodegraded tetracycline hydrochloride solution were recorded by a UV-vis spectroscopy (UV2450).

Data availability statement. The datasets generated during and/or analyzed during the current study are available from the corresponding author on reasonable request.

References

1. Shearer, C. J., Cherevan, A. & Eder, D. Application and future challenges of functional nanocarbon hybrids. *Adv. Mater.* **26**, 2295–2318 (2014).
2. Liu, K. *et al.* Nitrogen-doping induced oxygen divacancies in freestanding molybdenum trioxide single-layers boosting electrocatalytic hydrogen evolution. *Nano Energy* **30**, 810–817 (2016).
3. Scully, J. P. & Zhou, H.-C. Enhancing amine-supported materials for ambient air capture. *Angew. Chem., Int. Ed.* **51**, 12660–12661 (2012).
4. Nadi, R. *et al.* Performance of nano-carbon loaded polymer composites: Dimensionality matters. *Carbon* **126**, 410–418 (2018).
5. Peng, K., Fu, L., Ouyang, J. & Yang, H. Emerging parallel dual 2D composites: Natural clay mineral hybridizing MoS₂ and interfacial structure. *Adv. Funct. Mater.* **26**, 2666–2675 (2016).
6. Li, X. & Peng, K. Hydrothermal synthesis of MoS₂ nanosheet/palygorskite nanofiber hybrid nanostructures for enhanced catalytic activity. *Appl. Clay Sci.* **162**, 175–181 (2018).
7. Tran-Cong-Miyata, Q., Nishigami, S., Ito, T., Komatsu, S. & Norisuye, T. Controlling the morphology of polymer blends using periodic irradiation. *Nat. Mater.* **3**, 448–451 (2004).
8. Sun, X. *et al.* Active morphology control for concomitant long distance Spin transport and photoresponse in a single organic device. *Adv. Mater.* **28**, 2609–2615 (2016).
9. Li, X. *et al.* Facile synthesis of wormhole-like mesoporous tin oxide via evaporation-induced self-assembly and the enhanced gas-sensing properties. *Nanoscale Res. Lett.* **13**, 14 (2018).
10. Peng, K., Fu, L., Li, X., Ouyang, J. & Yang, H. Stearic acid modified montmorillonite as emerging microcapsules for thermal energy storage. *Appl. Clay Sci.* **138**, 100–106 (2017).

11. Li, X. & peng, k. MoSe₂/montmorillonite composite nanosheets: Hydrothermal synthesis, structural characteristics and enhanced photocatalytic activity. *Minerals-Basel* **8**, 268 (2018).
12. Sun, W. *et al.* 3D ZnIn₂S₄ nanosheet/TiO₂ nanowire arrays and their efficient photocathodic protection for 304 stainless steel. *Appl. Surf. Sci.* **434**, 1030–1039 (2018).
13. Doan, M.-H. *et al.* Charge transport in MoS₂/WSe₂ van der waals heterostructure with tunable inversion layer. *ACS Nano* **11**, 3832–3840 (2017).
14. Peng, K., Fu, L., Yang, H., Ouyang, J. & Tang, A. Hierarchical MoS₂ intercalated clay hybrid nanosheets with enhanced catalytic activity. *Nano Res.* **10**, 570–583 (2017).
15. Liu, X., Su, Y., Zhao, Q., Du, C. & Liu, Z. Constructing Bi₂O₃/Cl₁₀/BiOCl heterojunction via a simple thermal annealing route for achieving enhanced photocatalytic activity and selectivity. *Sci. Rep.* **6**, 28689 (2016).
16. Peng, K. & Yang, H. Carbon hybridized montmorillonite nanosheets: preparation, structural evolution and enhanced adsorption performance. *Chem. Commun.* **53**, 6085–6088 (2017).
17. Jia, X. *et al.* Transforming type-I to type-II heterostructure photocatalyst via energy band engineering: A case study of I-BiOCl/I-BiOBr. *Appl. Catal., B* **204**, 505–514 (2017).
18. Peng, K., Fu, L., Yang, H. & Ouyang, J. Perovskite LaFeO₃/montmorillonite nanocomposites: synthesis, interface characteristics and enhanced photocatalytic activity. *Sci. Rep.* **6** (2016).
19. Yang, J. *et al.* A comparative study on the photocatalytic behavior of graphene-TiO₂ nanostructures: Effect of TiO₂ dimensionality on interfacial charge transfer. *Chem. Eng. J.* **334**, 907–921 (2018).
20. Meshram, S. P., Adhyapak, P. V., Mulik, U. P. & Amalnerkar, D. P. Facile synthesis of CuO nanomorphs and their morphology dependent sunlight driven photocatalytic properties. *Chem. Eng. J.* **204–206**, 158–168 (2012).
21. Nguyen-Phan, T.-D. & Shin, E. W. Morphological effect of TiO₂ catalysts on photocatalytic degradation of methylene blue. *J. Ind. Eng. Chem.* **17**, 397–400 (2011).
22. Carrillo, A. I., Serrano, E., Luque, R. & García-Martínez, J. Microwave-assisted catalysis by iron oxide nanoparticles on MCM-41: Effect of the support morphology. *Appl. Catal., A* **453**, 383–390 (2013).
23. Abbaraju, P. L. *et al.* Asymmetric mesoporous silica nanoparticles as potent and safe immunoadjuvants provoke high immune responses. *Chem. Commun.* **54**, 2020–2023 (2018).
24. Jia, D., Wang, K. & Huang, J. Filter paper derived nanofibrous silica-carbon composite as anodic material with enhanced lithium storage performance. *Chem. Eng. J.* **317**, 673–686 (2017).
25. Levi, G., Scolnik, Y. & Mastai, Y. Imprinting chirality in silica nanotubes by N-stearoyl-serine template. *ACS Appl. Mater. Interfaces* **8**, 23356–23361 (2016).
26. Lin, X. *et al.* Mn-N-C nanoreactor prepared through heating metalloporphyrin supported in mesoporous hollow silica spheres. *ACS Appl. Mater. Interfaces* **8**, 26809–26816 (2016).
27. Sun, Z., Li, H., Cui, G., Tian, Y. & Yan, S. Multifunctional magnetic core-shell dendritic mesoporous silica nanospheres decorated with tiny Ag nanoparticles as a highly active heterogeneous catalyst. *Appl. Surf. Sci.* **360**, 252–262 (2016).
28. Li, X. & Tang, A. Pd modified kaolinite nanocomposite as a hydrogenation catalyst. *RSC Adv.* **6**, 15585–15591 (2016).
29. Li, X., Ouyang, J., Zhou, Y. & Yang, H. Assembling strategy to synthesize Pd modified kaolin nanocomposites with different morphologies. *Sci. Rep.* **5**, 13763 (2015).
30. Zhang, Y., Gan, H. & Zhang, G. A novel mixed-phase TiO₂/kaolinite composites and their photocatalytic activity for degradation of organic contaminants. *Chem. Eng. J.* **172**, 936–943 (2011).
31. Hai, Y. *et al.* Modification of acid-activated kaolinite with TiO₂ and its use for the removal of azo dyes. *Appl. Clay Sci.* **114**, 558–567 (2015).
32. Mamulová Kutlákova, K. *et al.* Preparation and characterization of photoactive composite kaolinite/TiO₂. *J. Hazard. Mater.* **188**, 212–220 (2011).
33. Li, X., Fu, L., Ouyang, J. & Yang, H. Microwave-assisted synthesis and interfacial features of CdS/kaolinite nanocomposite. *Colloid. Surface. A* **443**, 72–79 (2014).
34. Zhou, F., Yan, C., Wang, H., Zhou, S. & Komarneni, S. Sepiolite-TiO₂ nanocomposites for photocatalysis: Synthesis by microwave hydrothermal treatment versus calcination. *Appl. Clay Sci.* **146**, 246–253 (2017).
35. Li, X., Yang, Q., Jing, Q., Yang, H. & Chang, S. Chitosan modified halloysite nanotubes as emerging porous microspheres for drug carrier. *Appl. Clay Sci.* **126**, 306–312 (2016).
36. Li, X. & Yang, H. Pd hybridizing ZnO/kaolinite nanocomposites: Synthesis, microstructure, and enhanced photocatalytic property. *Appl. Clay Sci.* **100**, 43–49 (2014).
37. Chen, Y. & Liu, K. Preparation and characterization of nitrogen-doped TiO₂/diatomite integrated photocatalytic pellet for the adsorption-degradation of tetracycline hydrochloride using visible light. *Chem. Eng. J.* **302**, 682–696 (2016).
38. Chen, Y. & Liu, K. Fabrication of Ce/N co-doped TiO₂/diatomite granule catalyst and its improved visible-light-driven photoactivity. *J. Hazard. Mater.* **324**, 139–150 (2017).
39. Zhang, Y. *et al.* Substitutional doping for aluminosilicate mineral and superior water splitting performance. *Nanoscale Res. Lett.* **12**, 456 (2017).
40. Shi, Y. *et al.* Palygorskite supported BiVO₄ photocatalyst for tetracycline hydrochloride removal. *Appl. Clay Sci.* **137**, 249–258 (2017).
41. Szczepanik, B. Photocatalytic degradation of organic contaminants over clay-TiO₂ nanocomposites: A review. *Appl. Clay Sci.* **141**, 227–239 (2017).

Acknowledgements

This work was supported by the National Natural Science Foundation of China (51704030), the China Postdoctoral Science Foundation (2017M610617, 2018T111054, 2017M623182), Shaanxi Postdoctoral Science Foundation (2017BSHEDZZ10), the Special Fund for Basic Science Research of Central Colleges of Chang'an University (310831171002, 300102318402), and Young Talent fund of University Association for Science and Technology in Shaanxi, China (20180411).

Author Contributions

X.Y.L. conceived the project and wrote the final paper. X.Y.L. wrote initial drafts of the work. X.Y.L. and K.P. designed the experiments, synthesized and characterized the materials, K.P., H.X.C. and Z.J.W. analyzed the data. All authors discussed the results and commented on the manuscript.

Additional Information

Competing Interests: The authors declare no competing interests.

Publisher's note: Springer Nature remains neutral with regard to jurisdictional claims in published maps and institutional affiliations.



Open Access This article is licensed under a Creative Commons Attribution 4.0 International License, which permits use, sharing, adaptation, distribution and reproduction in any medium or format, as long as you give appropriate credit to the original author(s) and the source, provide a link to the Creative Commons license, and indicate if changes were made. The images or other third party material in this article are included in the article's Creative Commons license, unless indicated otherwise in a credit line to the material. If material is not included in the article's Creative Commons license and your intended use is not permitted by statutory regulation or exceeds the permitted use, you will need to obtain permission directly from the copyright holder. To view a copy of this license, visit <http://creativecommons.org/licenses/by/4.0/>.

© The Author(s) 2018